IOP PUBLISHING JOURNAL OF MICROMECHANICS AND MICROENGINEERING

J. Micromech. Microeng. **22** (2012) 105012 (9pp) doi:10.1088/0960-1317/22/10/105012

A high-bandwidth electromagnetic MEMS motion stage for scanning applications

Young-Man Choi[1], **Jason J Gorman, Nicholas G Dagalakis, Seung Ho Yang, Yongsik Kim and Jae Myung Yoo**

Intelligent Systems Division, Engineering Laboratory, National Institute of Standards and Technology, Gaithersburg, MD 20899, USA

E-mail: ymchoi@kimm.re.kr

Received 8 December 2011, in final form 14 June 2012
Published 23 August 2012
Online at stacks.iop.org/JMM/22/105012

Abstract

This paper presents the design, fabrication methods and experimental results for a MEMS-based out-of-plane electromagnetic motion stage for scanning applications. The combination of electromagnetic actuation and a flexure-supported platform provides linear bidirectional motion with high precision. A planar microcoil and a permanent magnet are used to generate a Lorentz force, which drives the flexure-supported platform. The copper microcoil is electroplated on a silicon substrate and the platform is fabricated through silicon bulk micromachining of a silicon-on-insulator wafer. The resonant frequency of the fabricated motion stage is approximately 2.0 kHz, which results in an open-loop control bandwidth greater than 500 Hz. Experimental results verify that the stage has highly linear bidirectional motion with negligible hysteresis and nonlinearity over a $\pm$ 2.7 μm range. Additionally, excellent high-frequency tracking performance is demonstrated using open-loop control, with a tracking error below 6.5 nm RMS for scan rates up to 200 Hz.

(Some figures may appear in colour only in the online journal)

1. Introduction

Highly precise and stable motion stages are essential for many small-scale applications including scanning probe microscopy [1] and read/write heads for data storage drives [2] (see [3] for an overview). As the required size of these mechanisms continues to get smaller, motion stages must be miniaturized using microelectromechanical systems (MEMS) technologies [4–7]. In addition to small size, these applications typically require high bandwidth, reliable motion accuracy and sufficient motion range. High-bandwidth vertical scanning in particular is critical for scanning probes and read/write heads. For example, a vertical motion stage used in atomic force microscopy (AFM) must be able to control the interaction between a cantilever probe and sample with subnanometer precision while quickly reacting to changes in the surface topography as the sample is scanned [8]. In this application, the motion stage must be significantly stiffer than the AFM cantilever, which is generally below 50 N m^{-1}, to ensure that the measured atomic force is transmitted to the cantilever and not through the motion stage. Additionally, the motion bandwidth of the MEMS motion stage must be equivalent to or better than that of macroscale motion stages used in this application, which is typically above 1 kHz. The size requirement is dependent on the particular application but in general, smaller is better because it enables the use of arrays of motion stages with fine pitch. Unlike many other MEMS applications, the required motion range is not a significant challenge here since a few micrometers is adequate for most scanning probe and read/write head systems. This paper focuses on the development of a vertical MEMS motion stage that can satisfy these requirements.

Among the many MEMS actuation methods available, electromagnetic actuation based on the Lorentz force is

[1] Y.-M. Choi was at the National Institute of Standards and Technology, Gaithersburg, MD, USA at the time of this research. He is now at the Korean Institute for Machinery and Materials, Daejeon, Korea.

 © 2012 IOP Publishing Ltd Printed in the UK & the USA

particularly well suited for the vertical MEMS motion stage because it provides linear motion, has a fast response time, generates a large force in a small area and typically operates with voltages below 5 V. Other common actuation methods, such as electrostatic, thermal and piezoelectric, do not compare favorably with respect to one or more of these metrics (e.g. electrostatic—nonlinear, high voltage; thermal—slow response time; piezoelectric—hysteresis, difficult to deposit materials). A number of electromagnetic MEMS actuator designs have been reported in the literature over the last two decades [9–17]. However, none of these mechanisms simultaneously meet the requirements discussed above in terms of size, stiffness and bandwidth. This claim will be discussed in more detail later in the paper. As a result, a vertical (out-of-plane) motion stage based on the Lorentz force actuation principle developed by others [9–17] has been designed with modifications to the microcoil, flexure mechanism and magnet in order to meet the desired specifications. The motion stage can perform bidirectional displacement that is proportional to the input current and can be controlled with high precision, even with open-loop operation.

The design of the motion stage is described in section 2, including numerical analysis of the electromagnetic forces. The fabrication procedures for the microcoil and flexure-supported platform are then described in section 3. Experimental results for quasi-static motion and dynamic scanning are presented in section 4 to demonstrate the performance of the motion stage. A discussion on the performance of this actuator with respect to previous Lorentz force actuators is provided in section 5. This is followed by conclusions on the actuator design.

2. Motion stage design

In general, most electromagnetic MEMS actuators consist of a microcoil, a magnet and a flexure mechanism that guides the motion of either the magnet or microcoil [9–17]. The forces between the magnet and microcoil are controlled by the coil current while the resulting displacement is dependent on the stiffness of the flexure mechanism. Some of the design considerations for these three components (microcoil, magnet and flexure mechanism) are discussed in the following.

An electromagnetic coil generates two force components with the magnet, the magneto-static force and the Lorentz force. The relative magnitude of these forces is determined by the configuration of the coil and its position with respect to the magnet. Solenoid actuators use multiturn, multilayered coils to maximize the magneto-static force. However, it is difficult to fabricate multilayered coils using microfabrication processes in comparison to planar single-layer microcoils. Although a single-layer micromachined planar coil typically cannot generate a large enough magneto-static force for actuation, the Lorentz force can be used by properly designing the spatial interaction between the magnet and the magnetic field generated by the coil [18–20]. Lorentz force actuation using a single-layer coil has previously been shown to be more than adequate for MEMS actuation by a number of researchers [9, 10, 12–17]. The biggest advantages of Lorentz force actuators are that they are bidirectional and have linear characteristics, which is critical from the viewpoint of precision motion control.

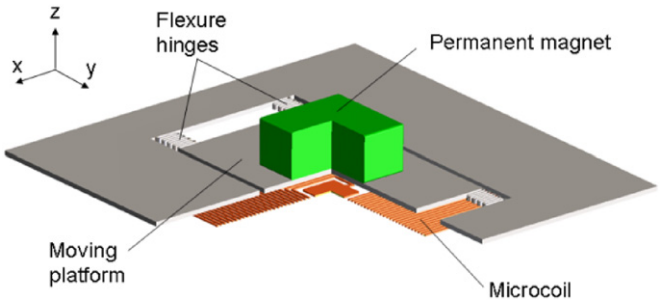

Figure 1. Design concept for the electromagnetic MEMS motion stage (partially sectioned).

Previous electromagnetic MEMS actuator designs have used two types of magnets, external permanent magnets that are integrated with the MEMS structure through assembly [9, 12] and deposited magnets that are integrated into the fabrication process [10, 11, 13–17]. External permanent magnets are easy to manufacture and capable of high magnetic strength, but their typical size in the past has been relatively large for MEMS (>1 mm) and they require precise microassembly techniques for integration with a mechanism. However, microscale permanent magnets have become commercially available within the last few years and automated microassembly methods have progressed to the point that assembled MEMS may become feasible (e.g., see [21]). Electroplated [11, 13–17] and polymer [10] magnets are compatible with many MEMS fabrication processes, but it is difficult to generate a strong magnetic field compared to external permanent magnets due to the thickness and quality of the deposited films. This tradeoff between high magnetic force and ease of system integration is one of the most important design decisions for electromagnetic MEMS.

In order to ensure precise motion of the actuator in the vertical direction and avoid contact between the magnet and microcoil, a flexure mechanism is necessary to provide compliant motion. Cantilevers have been widely used in MEMS actuators for this purpose [10, 11, 13–16], but they result in rotational errors rather than providing pure translational motion. As a result, symmetric flexure mechanisms that result in pure translation are required for precise motion control [9, 17]. Additionally, the flexure mechanism must be designed with a compliance that results in the specified travel range and resonant frequencies while restricting motion along the other axes.

Based on the considerations described above, an electromagnetic motion stage has been designed that consists of three parts: a planar microcoil, a flexure-supported platform and an external permanent magnet, as shown in figure 1. The microcoil has multiple spiral turns of conducting wire in a horizontal plane. Electromagnetic force is generated by running current through the microcoil while it is in the magnetic field of the permanent magnet, which drives the flexure-supported platform in the z-direction. Since the force

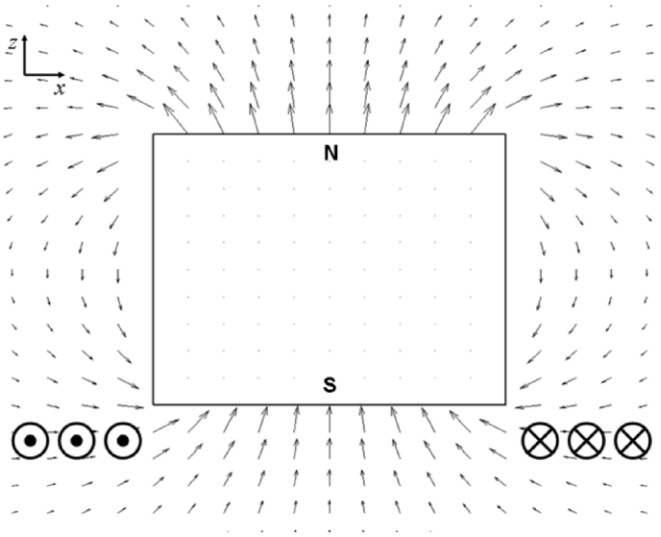

Figure 2. Vertical cross section of the magnetic flux around the permanent magnet and microcoil.

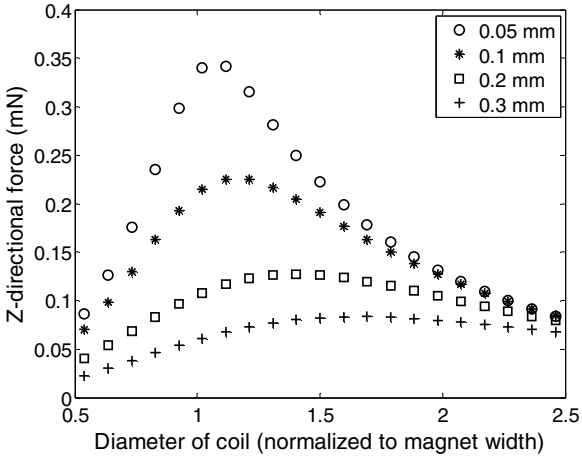

Figure 3. Lorentz force in the z-direction as a function of the location of the coil relative to the magnet, where the coil current is 1 A (vertical gap size ○: 0.05 mm, *: 0.1 mm, □: 0.2 mm, +: 0.3 mm).

capacity of the Lorentz force is relatively small, it is essential to create a horizontal magnetic field (x and y directions) such that the direction of the current flow is perpendicular to the magnetic field. As a result, the microcoil is designed to be square to match the selected permanent magnet. Though the permanent magnet is magnetized in the vertical direction (z-axis), the horizontal magnetic field is made radially around the fringes of the magnet, as shown in figure 2. Consequently, in order to generate a large Lorentz force, the microcoil should be positioned where the horizontal magnetic field is at its maximum. If the axis of the magnet and the axis of the microcoil are perfectly aligned, the other directional forces cancel each other due to symmetry.

The moving platform is supported by four flexures, one at each corner, to ensure rectilinear motion along the z-axis. Each flexure has a serpentine shape with either two or four turns. The serpentine flexure was selected because it has a small footprint, but adequate compliance along the z-axis to yield the desired motion range for the given electromagnetic force range. In order to achieve the desired compliance, the flexure-supported platform is fabricated using a silicon-on-insulator (SOI) MEMS fabrication process (details are discussed in section 3). The platform and flexures are 25 μm thick and the width of the flexure is 6 μm. The rectangular moving platform that carries the permanent magnet is 1460 μm $\times$ 840 μm. An external permanent magnet has been selected for this mechanism in order to maximize the actuation force, which is necessary to move the high stiffness platform.

To calculate the electromagnetic force on the motion stage, an analytical model was formulated. The magnetic field in the space outside of the permanent magnet was calculated using the surface current model [20] and Biot–Savart's law. The resulting force on the magnet was obtained by numerically integrating the Lorentz forces for infinitesimal coil elements due to the calculated magnetic field. This modeling approach is described in more detail in [22] and was implemented using MATLAB®[2] software.

Figure 3 shows the force generated along the z-axis by one coil turn for varying diameter of the coil relative to the magnet width as a function of the vertical gap between the magnet and coil, where the coil current is 1 A. The maximum force occurs when the coil diameter is slightly larger than the size of the magnet. As seen in figure 2, the horizontal magnetic field is maximized near this point, thereby resulting in high actuation force. Alternatively, the magnetic field close to the center of the coil is aligned to the z-axis and the intensity of the magnetic field drops off quickly when moving away from the magnet, resulting in low force for coil diameters in these regions. As the gap between the microcoil and magnet increases, the maximum force decreases in amplitude and its location moves away from the edge of the magnet. Similar results are presented in [18].

Since a planar microcoil comprises multiple turns of coil, it is best to locate as many coil turns near the edge of the magnet as possible. Thus, for a 500 μm cube magnet, the inner and outer diameters of the microcoil were chosen to be about 200 μm and 1400 μm, respectively. The outer diameter is selected to be almost three times larger than the magnet size so that it fully covers the fringes of the magnet. The dimensions and properties of the permanent magnet and the microcoil are shown in table 1. Figure 4 shows the total electromagnetic force along the z-axis for these system parameters as a function of gap size when the coil current is 1 A. As expected, the force along the z-axis is inversely proportional to the gap size, and the relationship is almost linear in the range of interest. At the nominal gap of 120 μm, the force is approximately 6.3 mN A^{-1}. If the motion travel range is ± 10 μm, the variation of the force over this range is approximately 6% of the nominal force.

[2] Certain commercial products and processes are identified in this paper to foster understanding. Such identification does not imply recommendation or endorsement by the National Institute of Standards and Technology, nor does it imply that the products and processes identified are necessarily the best available for the purpose.

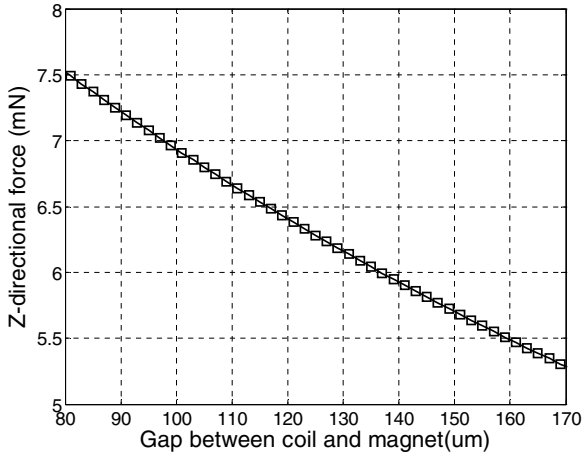

Figure 4. Force generated along the z-axis versus gap size between the microcoil and permanent magnet (microcoil current = 1 A).

Table 1. Properties of the permanent magnet and microcoil.

		Value	Unit
Magnet	Magnet size (W × T × H)	500 × 500 × 500	μm^3
	Remanence	1.45	T
	Mass	9.25×10^{-7}	kg
Microcoil	Wire cross section (W × H)	10 × 8	μm^2
	Coil pitch	24	μm
	Outer size	1422 × 1422	μm^2
	Number of turns	25	–
	Resistance	18.2	Ω
Nominal air gap		120	μm

3. Fabrication process

The microcoil and flexure-supported platform are fabricated on two separate chips and then assembled together with the permanent magnet. The microcoil is fabricated using a combination of thin film processing and electroplating, as shown in figure 5. Electroplating is well suited for microcoil fabrication because it can deposit high-aspect-ratio metal structures with micrometer-scale feature control, which provides thick coils that can pass sufficient current to generate the electromagnetic force required for the motion stage. Fabrication begins by coating a silicon wafer with an insulating layer of silicon dioxide. Next, a 0.5 μm thick Cu lead wire is deposited using a lift-off process and electron beam evaporation. A 1 μm thick silicon dioxide layer is then deposited for electrical isolation using plasma-enhanced chemical vapor deposition followed by patterning using photolithography and reactive ion etching. Next, a 0.5 μm thick layer of Cu is deposited by electron beam evaporation to provide a seed layer for electroplating. The coil geometry is then patterned using photolithography and a high-aspect-ratio photoresist (Megaposit^{TM} SPR^{TM}220-7, Rohm and Haas Electronic Materials) that is spun to a thickness of 10 μm. The Cu microcoils are then electroplated using a commercial system (IKo CLASSIC, ElectroChemical Systems, Inc.) to a thickness of 10 μm. The cross section of the coil was found to be highly uniform. Finally, the photoresist is removed with

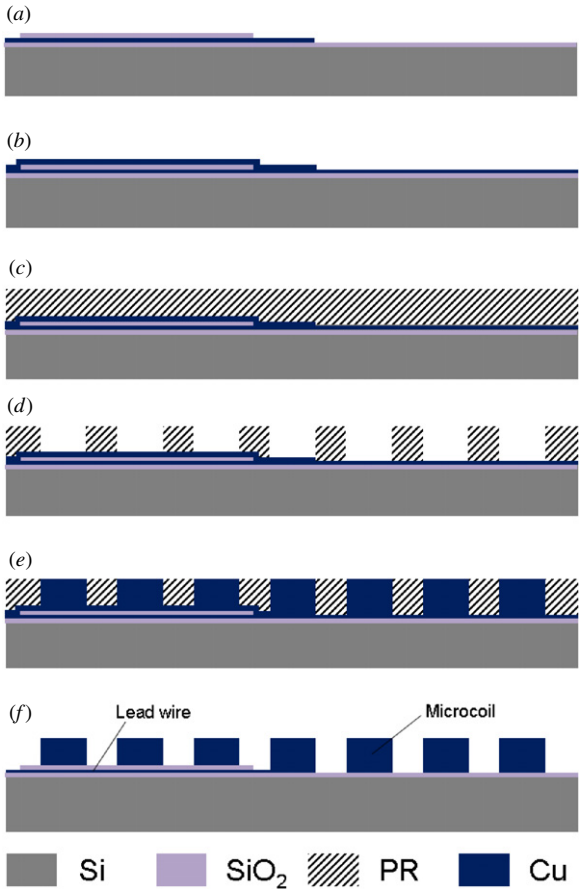

Figure 5. Fabrication process for the microcoil: (*a*) Cu lead wire and SiO_2 isolation layer patterning, (*b*) Cu seed layer deposition, (*c*) Spinning photoresist (PR), (*d*) photolithography patterning, (*e*) electroplating and (*f*) remove photoresist and Cu seed layer.

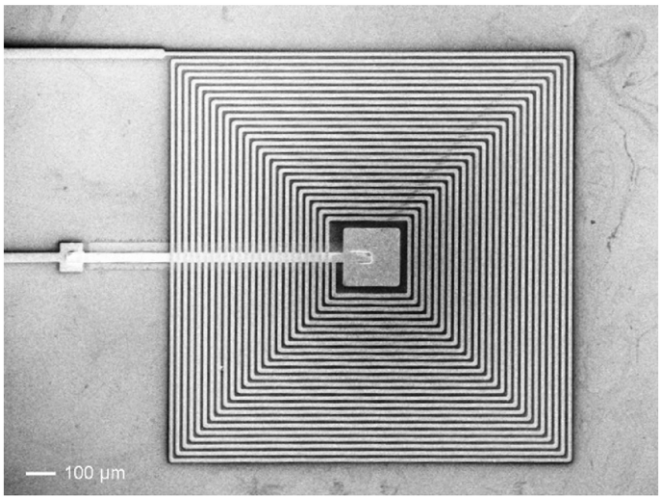

Figure 6. Fabricated microcoil (SEM image).

solvent and the Cu seed layer is removed with a wet etchant, resulting in functional microcoils with a thickness of 8 μm. Figure 6 shows a scanning electron microscope image of a fabricated microcoil.

The flexure-supported platform is fabricated using a standard silicon-on-insulator MEMS (SOI-MEMS) fabrication process. The SOI wafer has a 25 μm thick

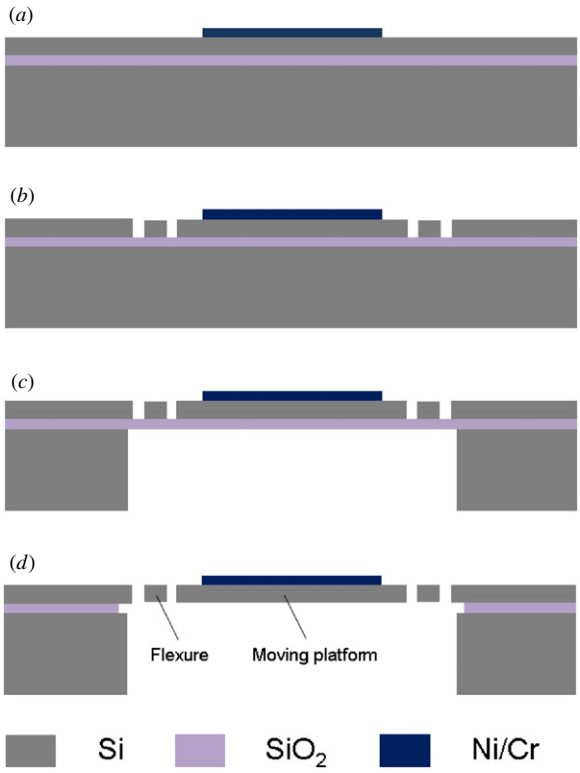

Figure 7. Fabrication process for flexure-supported platform: (*a*) Ni/Cr layers are deposited using liftoff, (*b*) platform shape is etched in the device layer using DRIE, (*c*) handle wafer is etched using DRIE and (*d*) platform is released by etching the SiO_2 layer in HF and critical point drying.

single-crystal Si device layer, a 1 μm silicon dioxide layer and a 400 μm handle wafer. The first step in the fabrication process is the deposition of a Ni pad centered on the platform, which is used to hold the permanent magnet on the platform before epoxy is applied. A lift-off process with electron beam evaporation is used to deposit Cr and Ni (Cr (50 nm)/Ni (500 nm)/Cr (50 nm)/Ni (500 nm)) (figure 7(*a*)). The first layer of Cr is used to promote adhesion of Ni while the second layer of Cr mitigates residual stress when depositing films of Ni above 500 nm. Next, the planar geometry of the flexure-supported platform is patterned using photolithography and deep reactive ion etching (DRIE) by etching down to the silicon dioxide layer (figure 7(*b*)). A protective photoresist is then applied to the topside. Next, the backside of the wafer is patterned using photolithography and DRIE is used to etch through the thickness of the handle wafer (figure 7(*c*)). Finally, the silicon dioxide layer below the platform is removed using a timed 49% HF etch and the release is completed with critical point drying.

Two chips, one with the microcoil and one with the platform, are manually assembled using an optical microscope for alignment. In order to achieve high electromagnetic force, the air gap between the platform and the microcoil must be minimized. Therefore, the platform is turned over such that the Ni layer faces the microcoil. Double-sided tape is used between the two chips to fix the assembly and provide a 120 μm air gap between the microcoil and the magnet. Epoxy-based photoresist SU-8 has also been used as a spacer layer between the two chips along with epoxy. A commercially

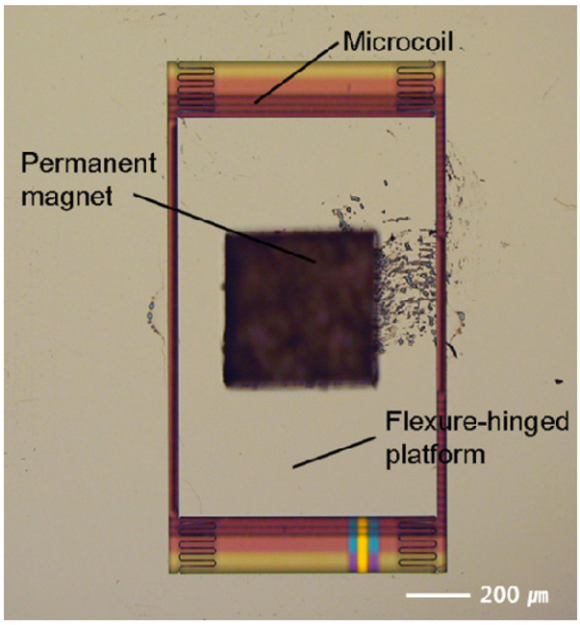

Figure 8. Assembled electromagnetic motion stage (top view).

available microscale NdFeB permanent magnet (N50 grade, BJA magnetics) is then assembled onto the backside of the platform where it is held by the Ni/Cr layer. A small bead of epoxy is applied to strengthen the bond. Figure 8 shows an optical image of an assembled motion stage.

4. Experimental results

In order to assess the static and dynamic performance of the motion stage, a position sensor has been developed based on the triangulation method, as shown in figure 9. The position sensor uses a diode laser and a quadrant photodiode to measure the out-of-plane displacement of the motion stage with bandwidth up to 10 kHz. To ensure good reflectivity, the backside of the platform is coated with a 50 nm thick layer of gold. The output of the position sensor was calibrated using an optical profiler (Wyko NT1100, Veeco). Figure 10 shows the bidirectional displacement of the motion stage as a function of the input voltage for a platform with two-turn serpentine flexures. The motion is linear and symmetric with an actuation gain of 0.66 μm V^{-1} and a linearity of 1% between -1 V and 1 V. The maximum input voltage before break-down of the microcoil was found to be $\pm$ 4.0 V ($\pm$ 0.22 A, max. power = 0.88 W) and the displacement range is approximately ± 2.7 μm.

The dynamic response of the motion stage in the frequency domain has also been measured, as shown in figure 11. The first resonance is observed at 2007 Hz with a quality factor of 30. The gain and phase are quite uniform up to approximately 1000 Hz, which makes open-loop operation possible in this range. Based on the first resonant frequency and the mass of the magnet and platform, the stiffness of the platform has been estimated to be 160 N m^{-1} assuming a harmonic oscillator response. The stiffness was also measured using a nanoindenter (TI 900 Triboindenter®, HYSITRON), yielding a value of 164 N m^{-1}, which matches closely with

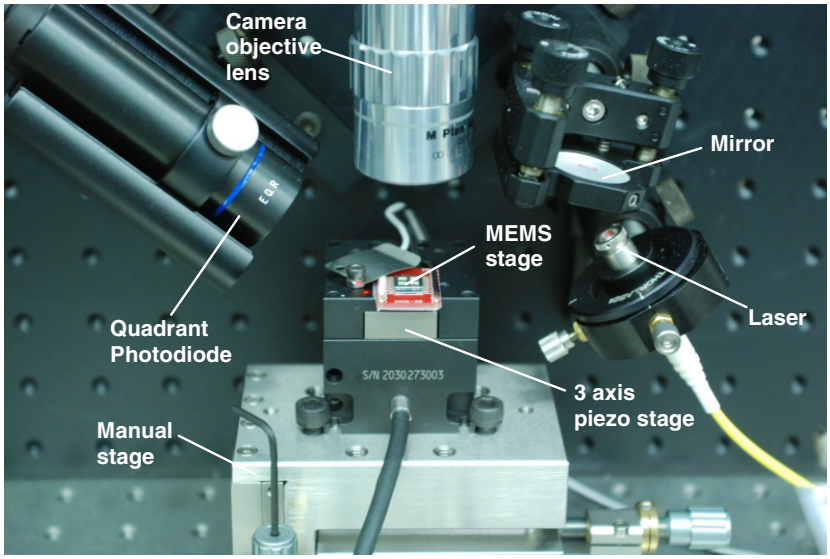

Figure 9. Experimental setup for characterizing the performance of the motion stage.

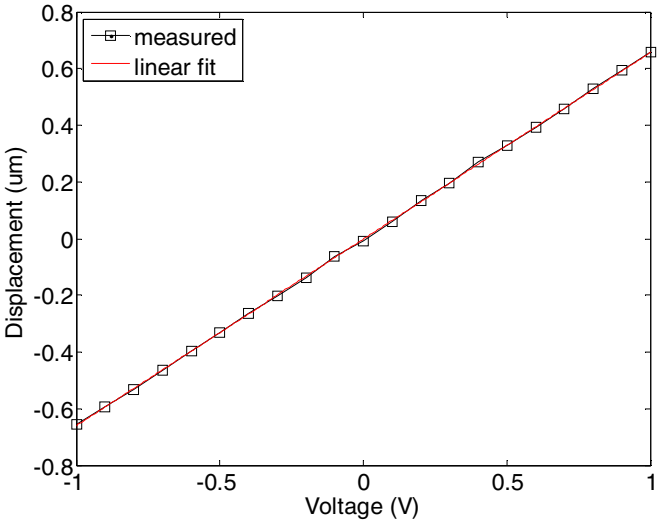

Figure 10. *z*-axis displacement versus input voltage.

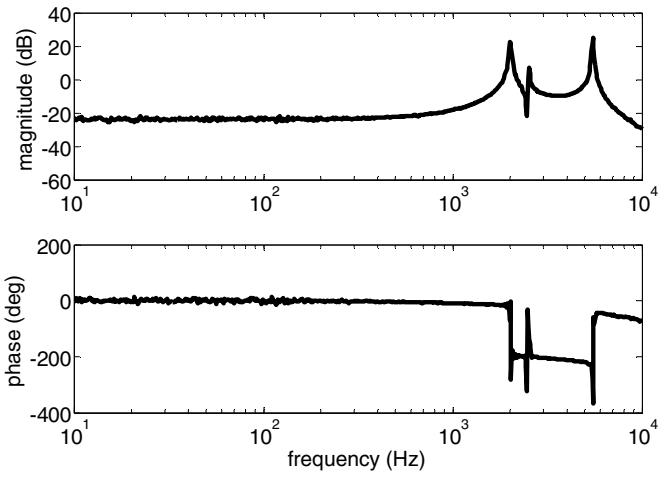

Figure 11. Frequency response of the motion stage.

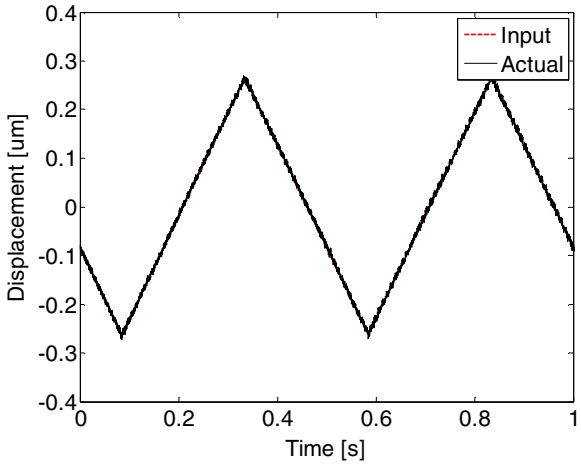

Figure 12. 2 Hz triangular open-loop actuation.

the estimated value. From the stiffness and the displacement gain, assuming that the coil resistance remains constant, the actual electromagnetic force per coil current is calculated as 1.97 mN A^{-1}, which is smaller than the estimated value (6.4 mN A^{-1}) in figure 4. Sources for the reduced force sensitivity include misalignment between the magnet and microcoil, imperfections in the magnet and microcoil, and magnetic losses caused by the Ni/Cr layer.

The proposed motion stage is suitable for high-frequency motion tracking because of its noncontact actuation, flexure-guided mechanism and linear response. As a result, the open-loop tracking performance for this mechanism has been evaluated. The stage demonstrates near-perfect tracking of a 2 Hz triangular trajectory without any vibration or nonlinearities with a tracking error below 4.4 nm RMS, as shown in figure 12. Figure 13 shows additional open-loop tracking results for sinusoidal trajectories at 10 Hz, 200 Hz and 2 kHz. At 10 Hz and 200 Hz, the tracking errors are 6.5 nm and 4.1 nm RMS, respectively. As the frequency of the sinusoidal trajectory is increased beyond 200 Hz, the open-loop gain increases until reaching the resonant frequency. However,

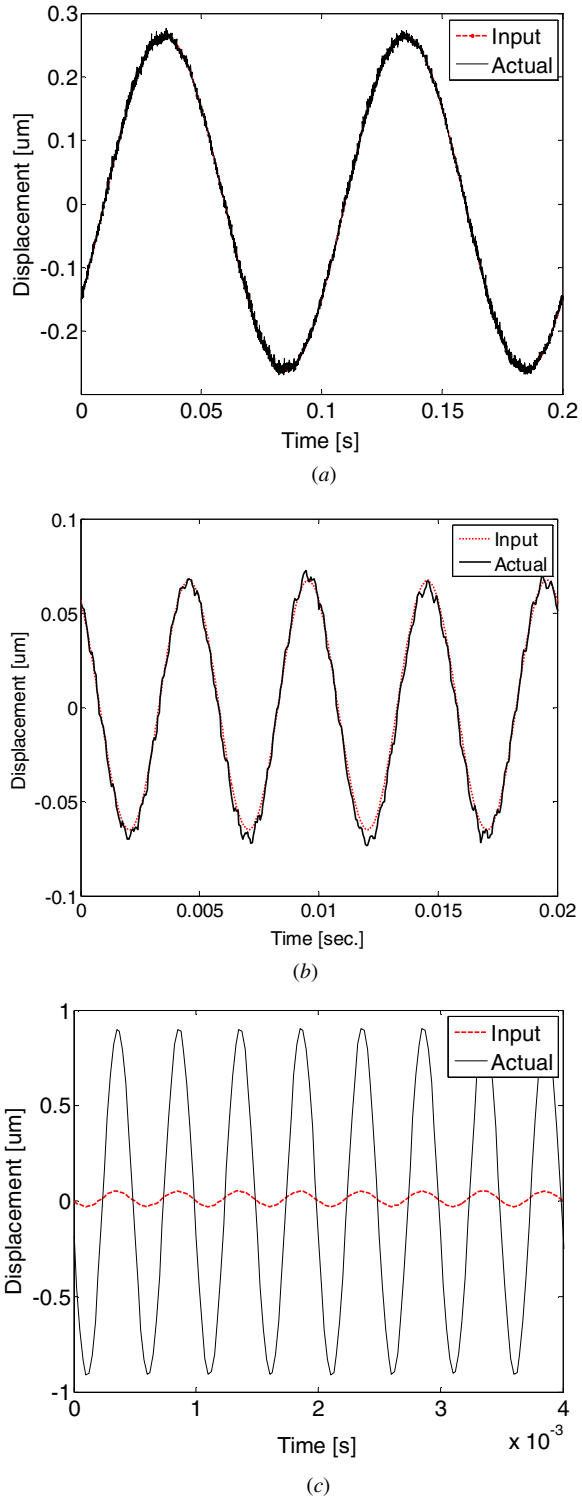

Figure 13. Sinusoidal open-loop actuation: (*a*) 10 Hz, (*b*) 200 Hz and (*c*) 2 kHz (in (*c*), the input command is magnified by 10 ×).

since the phase lag is relatively small, even at 2 kHz, as seen in figure 13(*c*), the open-loop response for frequencies above 200 Hz can easily be compensated using a simple feedfoward controller that attenuates the input signal to achieve the desired motion amplitude. Based on these results, the motion stage has been found to be highly precise with no signs of nonlinearity, hysteresis, or creep, verifying that the proposed design can be used for scanning applications.

5. Discussion

The goal of this work was to develop a microscale motion stage that has a stiffness that is significantly greater than 50 N m^{-1}, a motion bandwidth greater than 1 kHz and a motion range of a few micrometers, which has been achieved as demonstrated in the previous section. It was mentioned in the introduction that existing electromagnetic actuators did not meet these specifications. This claim is quantified in this section by comparing the presented motion stage with the most relevant examples previously reported in the literature. Table 2 provides this direct comparison in terms of the coil, magnet and mechanism area, the stage stiffness, the first resonant frequency and the force sensitivity, which is defined here as the force per unit current.

When comparing stage stiffness, it is clear that the stiffness of the actuators in [9–11, 14–16] and device II in [17] is at best 19.76 times smaller than the motion stage reported here. Therefore, these actuators are not suitable for the applications of interest in this paper. The only actuator that has a stiffness on the same order of magnitude as the specification is device I in [17]. Although device I is promising in terms of stiffness and resonant frequency, large current and power are necessary for actuation due to its low force sensitivity. Assuming that device I had a stiffness of 164 N m^{-1} in order to provide a direct comparison with our mechanism, 1.17 A of current and 4.38 W of power would be required to move 0.5 μm. In comparison, the motion stage reported here would require 0.026 A (45 times smaller) and 0.012 W (365 times smaller). This comparison is not meant to assert that any one of these designs is better than the other. Rather, it highlights the fact that previous research on electromagnetic MEMS actuators has focused on a very different part of the parameter design space than pursued in this paper and that it was necessary to redesign the standard Lorentz force actuator to achieve the required specifications.

It is also instructive to compare the motion stage presented here with a typical parallel plate electrostatic actuator, which at first glance is an obvious alternative for the applications of interest. The quasi-static relationship between the applied voltage and displacement of a parallel plate electrostatic actuator can be written as $k\,(g_0 - z) = \varepsilon_0 A V^2/2z^2$, where k is the stiffness of the actuator, g_0 is the undeflected gap between the plates, z is the gap between the plates, ε_0 is the permittivity of free space, A is the area of one plate and V is the applied voltage [23]. Electrostatic actuators are unidirectional and pull in occurs when the moving plate travels beyond one third of the undeflected gap. In order to compare the electromagnetic and electrostatic actuators, g_0 is set to 21.6 μm such that the equivalent motion range of 5.4 μm ($\pm$2.7 μm for the electromagnetic motion stage) is one quarter of the undeflected gap, providing a small buffer with the unstable region. Using the area of the flexure-suspended platform (1460 μm × 840 μm), an applied voltage of 207 V would be required to achieve the desired motion. Additionally, the area of the flexure-suspended platform could easily be reduced to 700 μm × 700 μm with negligible effect on the displacement of the electromagnetic motion stage. However, this change

Table 2. Comparison of electromagnetic MEMS actuators in terms of size, stiffness, resonant frequency and force sensitivity.

Parameter	[9]	[10]	[11]	[14–16]	[17] Device I	[17] Device II	Presented work
Coil area (mm^2)	33.64	153.76	32.67	0.4	0.13	0.38	2.02
Magnet area (mm^2)	2.25	12.57	4.00	0.2	0.13	0.38	0.25
Mechanism area (mm^2)	5.76	7.00	6.00	2.01	0.79	1.77	1.23
Stiffness ($N\ m^{-1}$)	8.30[a]	5.01[a]	0.64[a]	4.55	75.00	3.50	164.00
Resonant frequency (Hz)	94	41	–	300	16000	1470	2007
Force sensitivity ($mN\ A^{-1}$)	1.99[a]	0.77[a]	0.51[a]	1.08	0.07[a]	0.16[a]	1.97

[a] Estimated based on parameters provided in the reference.

would increase the actuation voltage for the electrostatic actuator to 327 V. The actuation voltage for the electrostatic actuator in both of these cases is too high to be of use in most applications due to the strong possibility of electrical breakdown of the materials and shorting caused by particulates and contact with samples, making the electromagnetic motion stage a better solution for the scanning probe and read/write head applications of interest in this paper.

Although the performance of the presented mechanism meets the desired specifications, there are a few simple modifications that could further improve its design. As mentioned above, the flexure-supported platform can be reduced down to 700 μm $\times$ 700 μm in area because it only needs to be big enough to support the magnet. This would increase the resonant frequency and decrease the bending of the platform during actuation. Additionally, the flexures should be redesigned to maximize the in-plane stiffness and to ensure that the first resonance is the out-of-plane mode that is used for actuation. It was determined through finite element analysis that the first resonance for the current design is an in-plane mode and the resonant frequency is approximately 30% smaller than the measured out-of-plane mode. However, the in-plane mode was not detected in our tests because the electromagnetic force is orthogonal to this mode. Even so, it is important that future designs optimize the flexures so that the in-plane mode is higher in frequency than the first out-of-plane mode.

6. Conclusion

The design, fabrication and experimental results for an out-of-plane bidirectional electromagnetic MEMS motion stage have been presented. Specifications for the stiffness, first resonant frequency and range of motion for the stage were determined based on applications of interest in scanning probe microscopy and data storage. These specifications were met by the implemented design and the motion of the stage has been shown to be linear with no detectable hysteresis over a range of $\pm$ 2.7 μm. Interestingly, when compared to other electromagnetic MEMS actuators based on the Lorentz force, the presented design is the only one that the authors are aware of that could meet the desired specifications. The defined specifications required development within a completely different part of the parameter design space for Lorentz force actuators compared to the more commonly explored applications, such as microscale pumps, valves and switches [14–17]. Due to the high first resonant frequency of the motion stage, precise open-loop controlled scanning up to 200 Hz was able to be demonstrated. Additionally, it appears that scanning up to 2 kHz is achievable with the addition of a simple open-loop controller to attenuate the motion amplitude as the resonant frequency is approached. These results demonstrate that electromagnetic MEMS motion stages have potential in enabling the next generation of high-speed scanning probe instruments and data storage systems.

Acknowledgments

Research performed in part in the NIST Center for Nanoscale Science and Technology (CNST) Nanofab user facility.

References

[1] Salapaka S, Sebastian A, Cleveland J P and Salapaka M V 2002 High bandwidth nano-positioner: a robust control approach *Rev. Sci. Instrum.* **73** 3232–41
[2] Soeno Y, Ichikawa S, Tsuna T, Sato Y and Sato I 1999 Piezoelectric piggy-back microactuator for hard disk drive *IEEE Trans. Magn.* **35** 983–9
[3] Hubbard N B, Culpepper M L and Howell L L 2006 Actuators for micropositioners and nanopositioners *Appl. Mech. Rev.* **59** 324–34
[4] Kim C-H and Kim Y-K 2002 Micro XY-stage using silicon on a glass substrate *J. Micromech. Microeng.* **17** 103–7
[5] Ando Y 2004 Development of three-dimensional electrostatic stages for scanning probe microscope *Sens. Actuators,* A **114** 285–91
[6] Bergna S, Gorman J J and Dagalakis N G 2005 Design and modeling of thermally actuated MEMS nanopositioners *Proc. ASME IMECE, (Orlando, FL) IMECE2005-82158* pp 561–68
[7] Liu X, Kim K and Sun Y 2007 A MEMS stage for 3-axis nanopositioning *J. Micromech. Microeng.* **17** 1796–802
[8] Meyer E, Hug H J and Bennewitz R 2004 *Scanning Probe Microscopy: The Lab on a Tip* (Berlin: Springer)
[9] Wagner B and Benecke W 1991 Microfabricated actuator with moving permanent magnet *Proc. IEEE MEMS Conf.* pp 27–32
[10] Lagorce L K, Brand O and Allen M G 1999 Magnetic microactuators based on polymer magnets *J. Microelectromech. Syst.* **8** 2–9
[11] Cho H J and Ahn C H 2002 A bidirectional magnetic microactuator using electroplated permanent magnet arrays *J. Microelectromech. Syst.* **11** 78–84
[12] Kim K H, Yoon H J, Jeong O C and Yang S S 2005 Fabrication and test of a micro electromagnetic actuator *Sensors Actuators* A **117** 8–16
[13] Pan C T and Shen S C 2005 Magnetically actuated bi-directional microactuators with permalloy and Fe/Pt hard magnet *J. Magn. Magn. Mater.* **285** 422–32

[14] Bintoro J S, Papania A D, Berthelot Y H and Hesketh P J 2005 Bidirectional electromagnetic microactuator with microcoil fabricated on a single wafer: static characteristics of membrane displacements *J. Micromech. Microeng.* **15** 1378–88

[15] Sutanto J, Papania A D, Berthelot Y H and Hesketh P J 2005 Dynamic characteristics of membrane displacement of a bidirectional electromagnetic microactuator with microcoil fabricated on a single wafer *Microelectron. Eng.* **82** 12–27

[16] Sutanto J, Hesketh P J and Berthelot Y H 2006 Static and dynamic responses of an electromagnetic bistable-bidirectional microactuator on a single silicon substrate *Sensors Actuators* A **132** 701–13

[17] Luharuka R, LeBlanc S, Bintoro J S, Berthelot Y H and Hesketh P J 2008 Simulated and experimental dynamic response characterization of an electromagnetic valve *Sensors Actuators* A **143** 399–408

[18] Feustel A, Krusemark O and Müller J 1998 Numerical simulation and optimization of planar electromagnetic actuators *Sensors Actuators* A **70** 276–82

[19] de Bhailís D, Murray C, Duffy M, Alderman J, Kelly G and Mathúna S C Ó 2000 Modelling and analysis of a magnetic microactuator *Sensors Actuators* A **81** 285–9

[20] Gou X.-F., Yang Y and Zheng X-J 2004 Analytic expression of magnetic field distribution of rectangular permanent magnets *Appl. Math. Mech.* **25** 297–306

[21] Wason J, Wen J T, Gorman J J and Dagalakis N G 2012 Automated multi-probe microassembly using vision feedback *IEEE Trans. Robot.* in press

[22] Choi Y-M, Lee M G, Gweon D-G and Jeong J 2009 A new magnetic bearing using Halbach magnet arrays for a magnetic levitation stage *Rev. Sci. Instrum.* **80** 045106

[23] Hung E S and Senturia S D 1999 Extending the travel range of analog-tuned electrostatic actuators *J. Microelectromech. Syst.* **8** 497–505